geosciences

Article

Fractal Dimension Analysis Applied to Soil CO_2 Fluxes in Campotosto's Seismic Area, Central Italy

Simone D'Incecco [1], Piero Di Carlo [1], Eleonora Aruffo [1], Nikolaos Chatzisavvas [2], Ermioni Petraki [3], Georgios Priniotakis [2], Ioannis Voyiatzis [3], Panayiotis H. Yannakopoulos [3] and Dimitrios Nikolopoulos [2,*]

1. Department of Psychological, Health & Territorial Sciences, University 'G. D'Annunzio' of Chieti-Pescara, via dei Vestini, 31, 66100 Chieti, Italy; simone.dincecco@unich.it (S.D.); piero.dicarlo@unich.it (P.D.C.); puppolola@gmail.com (E.A.)
2. Department of Industrial Design and Production Engineering, University of West Attica, Petrou Ralli & Thivon 250, GR122 44 Aigaleo, Greece; nikolaos.chatzisavvas@gmail.com (N.C.); gprin@uniwa.gr (G.P.)
3. Department of Computer Engineering, University of West Attica, Agiou Spyridonos, GR122 43 Aigaleo, Greece; epetraki@uniwa.gr (E.P.); voyageri@uniwa.gr (I.V.); pyian@uniwa.gr (P.H.Y.)

* Correspondence: dniko@uniwa.gr; Tel.: +30-210-5381338

Received: 10 April 2020; Accepted: 20 May 2020; Published: 17 June 2020

check for updates

Abstract: This article reports fractal dimension analysis applied to soil CO_2 fluxes measured in an Italian seismic area. The work was carried out with the use of a calibrated flux chamber unit. The fractal dimension (FD) from isotropic variograms was used as a method to understand related scale-dependent phenomena. The aim was to investigate the spatial variability of CO_2 flux measurements in four directions (horizontal, vertical, 45° and 135° directions) related to different distances between the measuring points and from a fault. High fractal dimension values were found ($2.5 \leq FD \leq 3.0$). These imply strong anti-persistent behavior near to and far from the fault. Lower fractal dimensions were addressed at longer distances from the fault.

Keywords: fractal dimension; CO_2 fluxes; seismic area

1. Introduction

Surveys of soil gas have been commonly used to trace buried faults and to study the behavior of endogenous gases of specific origins in the shallow environment (i.e., trace gases such as radon and helium, and carrier gases such as carbon dioxide, nitrogen, methane, etc.) [1–8] and have received significant attention over the last few years as earthquake precursors [6,9–15]. In addition, changes in stress/strain associated with seismic activity may force the migration of crustal fluid, in particular along active faults, thereby altering the geochemical characteristics of the surface fault zone [16–18]. The movement of these gasses by diffusion and/or advection along active faults will create flow anomalies, with concentrations substantially higher than the background levels; such anomalies may provide accurate information about the position and morphology of the shallow fracturing zone, as well as the permeability within the fault zone [3,4,7,19–21].

In recent years, geological, seismological, geophysical and geochemical knowledge has contributed to a much stronger, but far from complete, understanding of the link between faults and earthquakes in terms of space and time, with important advances in the analysis of seismic precursors applied to probabilistic seismic hazard assessment [12].

A fractal is a geometrically rough or broken structure that can be subdivided into sections, each of which is (at least approximately) a copy of the whole. Fractal geometry is the analysis of geometric forms that appear chaotic or irregular when compared to those of standard geometries (e.g., line, square, sphere, etc.), which exhibit extreme orderliness. Fractals may show invariant properties under reasonable contractions or dilations [22].

The authors in [23,24] asserted that phenomena with scale-dependent spatial variability can be studied through the concept of the fractal dimension. The technique has also been applied to non-continuous spatial and temporal phenomena [25]. According to [26], the fractal dimension applied to the characterization of soil can provide an estimation of the scale regularity and irregular behaviour. Scale dependency and spatial variability have been addressed in the relationship between CO_2 fluxes and soil attributes [27,28]. In addition, [29] reported that the spatial variability of CO_2 flux is partially subject to experimental semi-variogram adjustments, which must be properly selected. This subjectivity can be attributed to the dependence of the experimental semi-variogram on grid characteristics, such as the direction and sampling distance used at the experimental site [30,31]. Previous studies have used different range values of CO_2 fluxes for different locations, soil types and vegetation covers [32–35]. Certainly, new approaches and more research are needed to better understand the spatial variability of CO_2 fluxes at different scales [36]. Some studies were carried out to understand the fractal behavior in seismic areas [37,38]. According to [39,40], the CO_2 fluxes in seismic areas can be used to estimate the relationships between CO_2 gas emissions and seismic activity.

Accounting for the above findings, this paper focused on the study of the spatial analysis and variability of CO_2 flux from soil using fractal dimensions calculated with the semi-variogram method. The fractal characteristics of the underlying mechanisms that govern the spatial variability of CO_2 flux were delineated, and important information about the hidden long-lasting patterns of the Campotosto seismic area (Central Italy) were found and reported.

2. Methodology and Data Analysis

2.1. Experimental

The study area is located at Campotosto (42°55′ N and 13°38′ E), a small village approximately 20 km away from L'Aquila city, in the Abruzzo region (Central Italy, Figure 1). Abruzzo lies in the Apennine chain. In the vicinity of Campotosto, there is a significant active fault, the so called Mount Gorzano fault, of approximately 28 km length (Figure 2), a normal-type fault with WSW-dipping and a length-in-depth about 19.6 km [41–44]. Moreover, the rocks that outcrop in this study area are a flysh-type succession called the pre-evaporitic member of the Laga Formation [45]. This specific stratigraphic succession found in the study area is the arenaceous-pelitic (LAG4, lower Messinian [46]), characterized by the alternation of layers of sandstone and clay with relation $A/P > 1$ [46]. This is a strategical study area because is very near to active faults that generated big earthquakes on 24 August 2016 and also on 26 and 30 October 2016 in Central Italy [43,44].

The 37 CO_2 flux measurements were performed, independently, in two discrete phases, on 25 September 2019 and on 1 December 2019. Figure 3 presents all these 37 different measurements in the Campotosto area. During all the measurements, the climatic conditions were sunny without previous rain. Prior to data acquisition, superficial vegetation was removed in order to achieve the direct contact of the measuring device with the soil and rock underneath.

CO_2 fluxes from soil were measured by a flux chamber unit constructed at the University 'G. D'Annunzio' of Chieti-Pescara, Italy. The instrument consists of a cylindrical stainless steel container of 30 cm diameter and of 18 cm height (12.72 L volume-chamber). The unit was calibrated and tested for measurement accuracy. The calibration phase was implemented through the use of a laboratory-constructed system, which controlled the flow of various air and CO_2 mixtures (via a LabView program (National Instruments Corporation, Austin, TX, USA)), while concurrently measuring the flow with an external Mass Flow Controllers made by MKS Instrument, type 1179 Mass-Flo® Controller (Wilmington, MA, USA) and an internal CDM4160 (Figaro®) pre-calibrated module that was installed inside the flux chamber for carbon dioxide measurement (value range: 390–4000 ppm of CO_2 concentration).

The calibration factor of the flux chamber unit was calculated as the slope of the least-squares fit between the CO_2 concentrations measured by the chamber unit (internal controller) and the flow-driven CO_2 concentrations measured by the external units.

Figure 1. Map of study area in proximity to Campotosto in Central Italy. The figure presents the Mount Gorzano fault (red line) [43,44] and the main cities.

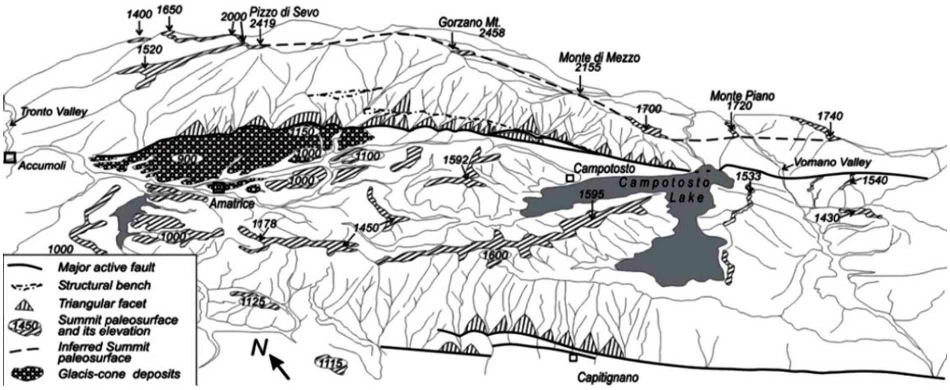

Figure 2. Geomorphological map of the study area. Map taken from [45].

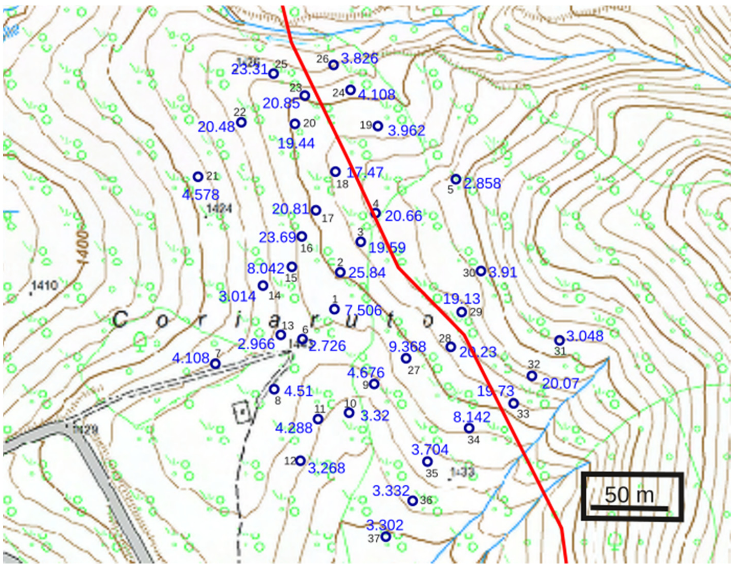

Figure 3. The map of the full set of measurements (flux values in ppm cm^{-2} s^{-1}), with the fault position [43,44] shown with a red line. The x axis represents the latitude from 42°33′23.436′′ N to 42°33′38.286′′ N, while the y axis represents the longitude from 13°22′58.962′′ E to 13°23′17.3832′′ E.

All the fluxes were calculated according to [47] by the equation:

$$\phi_{gas} = \alpha H_c \tag{1}$$

where α is the slope of the increase in gas concentration over time and H_c is the height of the chamber. Using Equation (1), the CO_2 fluxes were evaluated, and the relative results are shown in Figure 3 in ppm $cm^{-2}s^{-1}$.

The test phase was implemented to determine the quality of the CO_2 concentration measurements provided by the internal module of the unit. Two main tests were carried out: the first was implemented through increasing steps of the CO_2 concentrations driven to the chamber unit, and the second, through decreasing steps of CO_2 concentrations. Between each experimentation, adequate time was left for the CO_2 concentration values of the chamber to return to the corresponding baseline ones, which are usually around 400 ppm. In this way, the dead-time interval of the flux chamber unit was calculated, i.e., the time needed for the unit to return to its baseline recordings.

Proper sensors inside the chamber measured the temperature, pressure and humidity. Specifically, the LM35CAZ Precision Centigrade Temperature Sensor (National Semiconductor®, Santa Clara, CA, USA) was employed for temperature measurements, the XFPM-115KPA (Fujikura®, Tokyo, Japan) was used to measure atmospheric pressure, and the Honeywell® (Charlotte, NC, USA) HIH-4000 Series was utilized for relative humidity (RH) measurement. Moreover, the pressure inside and outside the chamber was balanced by a pressure compensation valve located at the top of the chamber. A rotating rod of carbon fibre and a gear motor (set to rotate less than 60 r/min) located inside the chamber reduces any bias effect due to gas stratification inside the chamber. The data were stored and saved every second with an Arduino board, mounted at the top of the chamber.

2.2. Mathematical Aspects

Spatial analysis based on the direction of measurements may provide important information regarding the fractal dimension (FD) and related scale-dependent phenomena [24,29,36]. Using experimental variogram analysis [36,48], it is possible to determine the fractal dimension according to Equation (2).

$$\hat{y}(h) = \frac{1}{2}N(h)\sum_{i=1}^{N(h)}[Z(x_i) - Z(x_i + h)]^2 \tag{2}$$

where $\hat{y}(h)$ is the semi-variance of points separated at a distance h, N is the number of pairs of points separated by h distance, $Z(x_i)$ is the value of the attribute at position x_i and $Z(x_i{+}h)$ is the value of the same attribute in position $x_i{+}h$.

The spatial structure of fractal surfaces can be described by means of a power law, as shown in the following relation:

$$\left|z(x) - z(x+h)\right| \propto h^H \tag{3}$$

where the location x has an attribute value z, with the separation distance h, and H is the fractal codimension or Hurst exponent [49]. If $0 < H \leq 1$, the fractal codimension can be defined as follows:

$$H = \mathrm{d} - \mathrm{FD} \tag{4}$$

where FD is the fractal dimension and d is the Euclidian dimension of the system in which the fractal distribution has been described. For lines, surfaces and volumes, $\mathrm{d} = 1, 2, 3$, respectively. Hence, for a distribution of a soil attribute, the fractal dimension is given by

$$\mathrm{FD} = 3 - H. \tag{5}$$

Comparing Equations (2) and (3), it is possible derive the semi-variance at a given scale as

$$\hat{y}(h) \propto h^{2H} \tag{6}$$

or as:

$$\log[\hat{y}(h)] \propto 2H \log[h]. \tag{7}$$

Through a logaritmic transformation, the slope of the experimental variogram can be calculated on the log–log scale as $2H$. The H exponent can then be obtained by means of a linear regression on the log–log graph by the following equation [23]:

$$\left(\frac{\log[\hat{y}(h)]}{2\log[h]}\right). \tag{8}$$

When $H = 0$, the value of FD is equal to 3, which represents the lack of a spatial variability structure, as there would be no relationship between the way the attribute varies in space and the distance between the points. In this case, there is no fractal dimension, and the methodology does not apply. However, when $0 < H < 1$, the fractal dimension has values that characterize the presence of spatial variability and dependence with h [29,31]. According to Equation (5), $2.0 \leq \text{FD} \leq 3.0$. When $2.0 \leq \text{FD} \leq 2.5$, there is a persistence behavior, while if $2.5 \leq \text{FD} \leq 3.0$, there is an anti-persistence behavior [29,36].

3. Results

The results of the calibration phase are given first. These results are very important because they verify the CO_2 measurements provided by the flux chamber unit and validate the method of the measurements. As aforementioned, two calibration factors were calculated, corresponding to increasing and decreasing steps of CO_2 driven concentrations. These are characteristically shown in Figure 4. The least-squares fit for Figure 4a is $y = 1.1008x + 1.4180$ with $R^2 = 0.9759$, and for Figure 4b, $y = 1.0075x + 2.2513$ with $R^2 = 0.9771$. Both lines have a very high square of the Spearman's correlation coefficient. This means that the flux chamber unit very accurately records the pre-determined CO_2 concentrations driven inside and originating from the external mass flow controllers. It is worth mentioning that the two mass flow controllers are good devices and that, therefore, the pre-determined driven CO_2 concentrations are very well defined. Hence, it is expected that in real-time situations, the CO_2 measurements will be accurate and reliable.

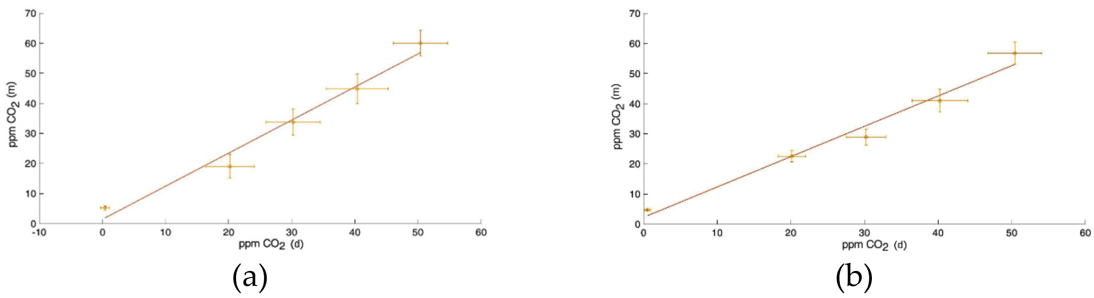

Figure 4. The best-line fits of the two tests: the first, (**a**) reports the increasing concentration test, while the second, (**b**), the decreasing concentration test. In both figures, the x axis (ppm CO_2 (d)) reports the CO_2 concentrations driven into the flux chamber unit, while the y axis (ppm CO_2 (m)) reports the CO_2 concentrations measured.

The measurements carried out in the Campotosto area to delineate the CO_2 flux profiles of the Mount Gorzano fault and its vicinity are shown in Figure 3 The map shows the 37 CO_2 flux measurements that were performed at various distances and positions from the fault. The maximum flux measured was 25.84 ppm cm^{-2} s^{-1}, and the minimum one was 2.858 ppm cm^{-2} s^{-1}. As can be observed from Figure 3, high CO_2 flux values (from 20 to 25 ppm cm^{-2} s^{-1}) are found near the fault, while, on the contrary, lower flux values (from 2 to 4 ppm cm^{-2} s^{-1}) can be observed in positions far from it. Tectonic fracture is related to the deformation pattern along the fault system and also facilitates a pathway for the CO_2 gasses [50–52], therefore leading to elevated fluxes near the fault. It should be noted that the soil CO_2 flux can be influenced by the rock type and by other parameters like chemical, physical and biological processes, including the soil temperature and atmospherical pressure [28,53]. Since the confirmation of the above observations needs further analysis, it is crucial that appropriate methods are employed. A significant approach towards this is monitoring the spatial fractal behavior of the CO_2 fluxes [29,36]. In association, it is significant to mention that the measurements were conducted following, as much as possible, the perpendicular direction (45° direction) with respect to the fault position. The scope was to acquire adequate profiles for statistical analyses. There are a variety of heights and spatial distributions of the measuring points in this study. The different distribution of heights is due to the morphology of the study area. Nevertheless, it seems that the surface profile of the fault is not a straight line (see Figure 3). Since the experimental approach of 45 degrees could not be followed exactly due to the morphology, further analysis in terms of the fractal semi-variogram method was attempted. In the following sections, this analysis is presented in detail.

As mentioned in the methods section and according to [36,54,55], the semi-variogram method is very efficient for the delineation of the hidden spatial trends in the CO_2 flux measurements. Since a spatial distribution of points has been achieved from the measurement procedure, the following alternative methods were employed for the calculation of fractal dimensions with the semi-variogram method: (1) reorganizing the flux measurements in four different directions (horizontal, vertical, 45° and 135°) via arbitrarily selecting pairs of measurements from the whole dataset (each pair indicated with a different ID number), so that all the selected series of pairs correspond to each one of the four directions; (2) reorganizing the series of pairs of 1), with reference to their intra-pair distance; and (3) arbitrary selecting pairs of measurements with different distances from the fault. The fractal dimensions with reference to the horizontal direction (Figure 5a) exhibited values of $1.5 \leq FD \leq 3.0$. The fractal dimensions with reference to the vertical direction (Figure 5b) exhibited values of $1.5 \leq FD \leq 3.0$. The fractal dimensions with reference to the 45° direction (Figure 5c) all had values over 2.5; in particular, certain fractal dimension values were found of $2.85 \leq FD \leq 2.9$ and $2.8 \leq FD \leq 2.85$. The fractal dimensions with reference to the 135° direction (Figure 5d) present values of $2.0 \leq FD \leq 3.0$.

Figure 6 presents fractal dimensions with reference to the distance in the four spatial directions. These are the distances between the various points that are spatially dispersed. Due to the scattering of the measurement points, there are a variety of distances from 20 m to 140 m. Note that Figure 6 is a reorganization of Figure 5 with reference to the distance and not to the ID number. Since there is no preferred direction in the above distances, Figure 6 has a different distribution of values in both the horizontal and vertical axes. It is very important to mention that all the fractal dimension values are over 2.5. This is a very significant finding that implies a strong fractal behavior of the CO_2-generating system in the spatial manner because the Hurst exponent (H) is between 0 and 0.5 [47,55]. This significant finding implies that when a high CO_2 concentration value is found, the next value will be low, and this tendency follows throughout the Campotosto area. Strong anti-persistent, long-lasting interaction exists. Observing that most high values are near the fault, the anti-persistence behavior justifies that the values after the fault will be low while the remaining values will have a trend of higher–lower values; all these values are lower than the corresponding values on the fault [56]. The fractal dimensions in the horizontal direction (Figure 6a) were all over 2.5; in particular, $FD \geq 2.9$ at 40 and 80 m; $2.8 \leq FD \leq 2.9$ at 50, 100 and 120 m; $2.6 \leq FD \leq 2.7$ at 30, 90 and 110 m; and $FD \leq 2.6$ at 60 m. The fractal dimensions in the vertical direction (Figure 6b) are all above 2.5; in particular, the FD is above or equal to 2.9 at 40 and 90 m; $2.8 \leq FD \leq 2.9$ at 60 m; $2.7 \leq FD \leq 2.8$ at 70, 90, 100 and 130 m; and $FD \leq 2.7$ at 140 m. The fractal dimensions in the 45° plane (Figure 6c) are all over 2.5; in particular, 2.7 ≤ FD ≤ 2.8 at 20, 30 and at 50 m; and 2.6 ≤ FD ≤ 2.7 at 40 and 60 m. The fractal dimensions in the 135° plane (Figure 6d) are between 2.90 and 2.98.

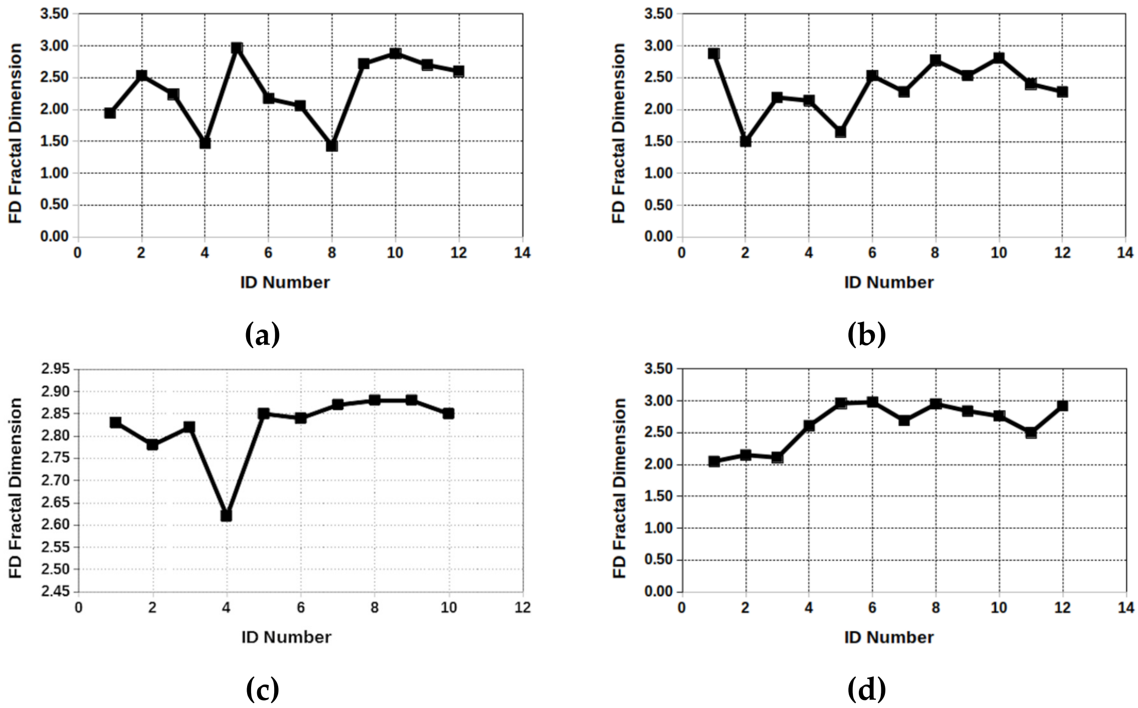

Figure 5. Fractal dimension (FD) values found in different planes in four spatial directions. (**a**) FD values in the horizontal plane. (**b**) FD values in the vertical plane. (**c**) FD values in the 45° plane. (**d**) FD values in the 135° plane.

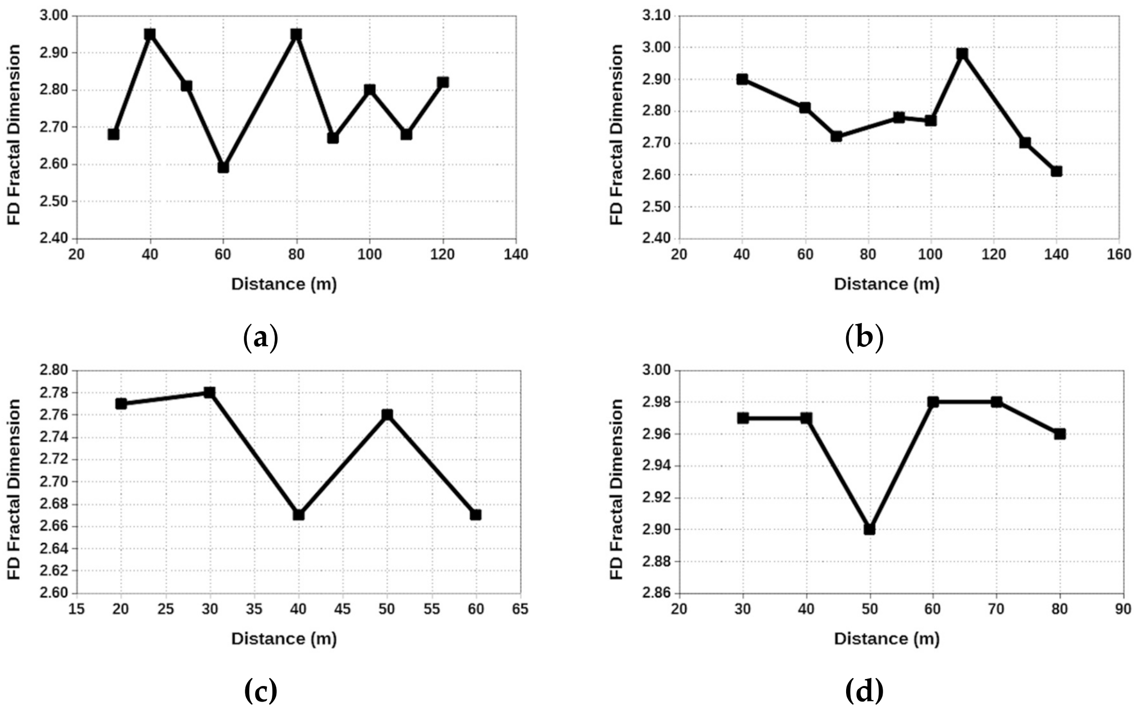

Figure 6. Fractal dimension (FD) values with different distances in the four spatial directions. (**a**) FD values in the horizontal direction. (**b**) FD values in the vertical direction. (**c**) FD values in the 45° direction. (**d**) FD values in the 135° direction.

This is characteristically shown in Figure 7 where the fractal dimensions with reference to the distance from the fault are presented. Figure 7 is the result of all the fractal dimension values taken at different positions from the fault. It is evident that the fractal dimension values away from the fault are lower. This finding verified the above facts in an alternative way. The fractal dimension values at greater distances are lower and, therefore, they follow the tendency of the CO_2 concentrations to exhibit anti-persistent behavior of lower intensity at greater distances. This means that the system goes away from strong anti-persistence and fractality when it is away from the fault; strong anti-persistence gradually diminishes. The significance of the strong anti-persistence behavior has been mentioned by several publications [56–60]. In the above publications, it was reported, in a multi-facet way, that the strong anti-persistent behavior, similarly to the strong persistence behavior, is a footprint of hidden activity in soil radon or environmental electromagnetic disturbances. According to [12], the radon in soil and CO_2 fluxes from soil may have similar origins inside the Earth's crust prior to seismic activity. It is the micro-crack branching, as possibly in the Mount Gorzano fault, that may act as a pathway for the increase in radon and CO_2 concentrations from soil. According to [61–63], the CO_2 fluxes increase inside the fault. All these aspects report different faces of the same aspect; the Mount Gorzano fault, as a seismic area, is associated with a strong CO_2 pathways and increased CO_2 concentration fluxes.

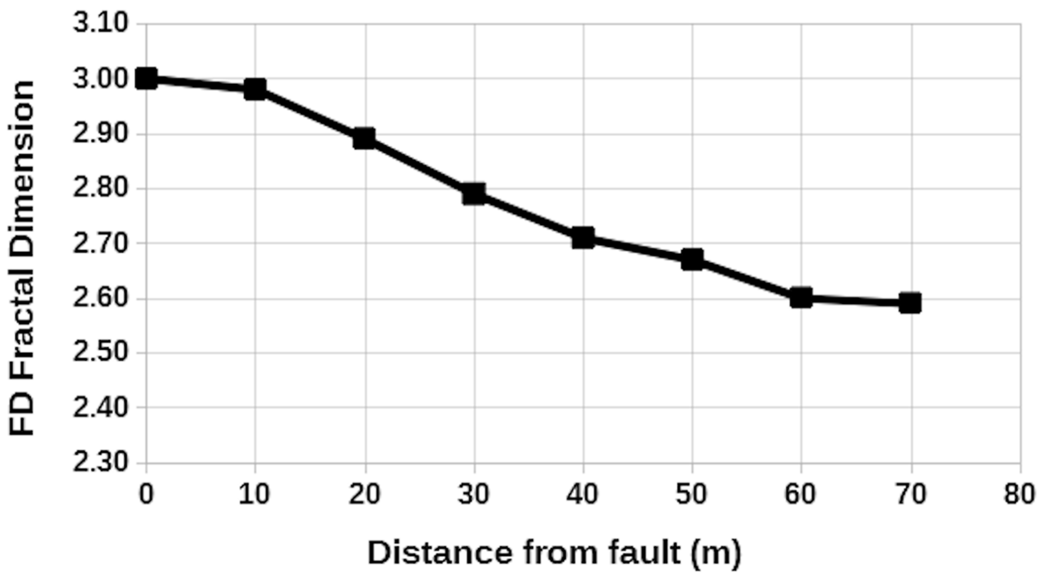

Figure 7. Fractal dimension values from the fault (at distance 0) to the different distances.

The above findings are verified by the results of other investigators. For example, [29] reported similar results showing comparable fractal dimension values between 2.5 and 3.0 of the spatial variability of soil CO_2 emissions, where it was shown that the fractal dimension decreased, as well, with the distance. This very important finding is similar to the tendency shown in Figure 7 and should be emphasized. This tendency of a decrease in the CO_2 values with the distance was also reported by these authors. This is an additional verification of the findings of this work. Additionally, [36] reported a similar range of fractal dimension values as in this work, where the fractal dimension values were between 2.5 and 3.0 from 5 m to 60 m, also decreasing with the distance. Furthermore, [55] calculated—also with the experimental variogram method, using the same equation as Equation (2) of this publication—the spatial variability of soil CO_2 fluxes. All the findings of this paper are comparable to those of other related papers, despite the fact that the sample size was not very high. More or less, the accuracy of the employed measuring device in conjunction with the modern methodological approach contributed towards this achievement.

4. Conclusions

The technique used for this work was an experimental semi-variogram that was applied to measuring CO_2 fluxes at the Campotosto seismic area (central Italy). Non-continuous spatial and temporal phenomena were addressed from the measurements.

The fractal dimension values at greater intra-distances and greater distances from the fault are lower and, therefore, they follow the tendencies of the CO_2 concentrations, to exhibit anti-persistent behavior of lower intensity at greater distances.

The fractal dimensions of this work are within the value ranges reported in similar work.

Author Contributions: Conceptualization, S.D., N.C., D.N.; Data curation, P.D.C. and E.A.; Formal analysis, D.N., E.P.; Investigation, S.D., P.D.C., E.A.; Methodology, D.N., I.V.; Resources, G.P.; Software, D.N. and N.C.; Supervision, D.N., P.D.C. and I.V.; Visualization, D.N.; Writing—original draft, S.D. and N.C.; Writing—review & editing, D.N., E.P., P.H.Y. and G.P. All authors have read and agreed to the published version of the manuscript.

Funding: This research received no external funding.

Conflicts of Interest: The authors declare no conflict of interest.

References

1. King, C.Y. Impulsive radon emanation on a creeping segment of the San Andreas fault, California. *Pure Appl. Geophys.* **1985**, *122*, 340–352. [CrossRef]
2. Ciotoli, G.; Guerra, M.; Lombardi, S.; Vittori, E. Soil gas survey for tracing seismogenic faults: A case study in the Fucino basin, Central Italy. *J. Geophys. Res.* **1998**, *103*, 23781–23794. [CrossRef]
3. Baubron, J.C.; Rigo, A.; Toutain, J.P. Soil gas profiles as a tool to characterize active tectonic areas: The Jaut Pass example (Pyrenees, France). *Earth Planet. Sci. Lett.* **2002**, *196*, 69–81. [CrossRef]
4. Ciotoli, G.; Lombardi, S.; Annunziatellis, A. Geostatistical analysis of soil gas data in a high seismic intermontane basin: Fucino Plain, central Italy. *J. Geophys. Res.* **2007**, *112*, B05407. [CrossRef]
5. Fu, C.C.; Yang, T.F.; Du, J.; Walia, V.; Chen, Y.G. Variations of helium and radon concentrations in soil gases from an active fault zone in Southern Taiwan. *Radiat. Meas.* **2008**, *43*, S348–S352. [CrossRef]
6. Walia, V.; Yang, T.; Hong, W.; Lin, S.; Fu, C. Geochemical variation of soil–gas composition for fault trace and earthquake precursory studies along the Hsincheng fault in NW Taiwan. *Appl. Radiat. Isot.* **2009**, *67*, 1855–1863. [CrossRef]
7. Bigi, S.; Beaubien, S.E.; Ciotoli, G.; D'Ambrogi, C.; Doglioni, C.; Ferrante, V.; Lombardi, S.; Milli, S.; Orlando, L.; Ruggiero, L.; et al. Mantle-derived CO_2 migration along active faults within an extensional basin margin (Fiumicino, Rome, Italy). *Tectonophysics* **2014**, *637*, 137–149. [CrossRef]
8. Ciotoli, G.; Sciarra, A.; Ruggiero, L.; Annunziatellis, A.; Bigi, S. Soil gas geochemical behaviour across buried and exposed faults during the 24th August 2016 central Italy earthquake. *Ann. Geophys.* **2016**, *59*. [CrossRef]
9. Wakita, H.; Nakamura, Y.; Notsu, K.; Noguchi, M.; Asada, T. Radon anomaly: A possible precursor to the 1978 Izu-Oshima-kinkai earthquake. *Science* **1980**, *207*, 882–883. [CrossRef]
10. Reddy, D.V.; Sukhija, B.S.; Nagabhushanam, P.; Kumar, D. A clear case of radon anomaly associated with a microearthquake event in a stable continental region. *Geophys. Res. Lett.* **2004**, *31*, L10609. [CrossRef]
11. Perez, N.M.; Hernandez, P.A.; Padron, E.; Melian, G.; Marrero, R. Precursory Subsurface ^{222}Rn and ^{220}Rn Degassing Signatures of the 2004 Seismic Crisis at Tenerife, Canary Islands. *Pure Appl. Geophys.* **2007**, *164*, 2431–2448. [CrossRef]
12. Cicerone, R.; Ebel, J.E.; Britton, J. A systematic compilation of earthquake precursors. *Tectonophysics* **2009**, *476*, 371–396. [CrossRef]
13. Ghosh, D.; Deb, A.; Sengupta, R. Anomalous radon emission as precursor of earthquake. *J. Appl. Geophys.* **2009**, *69*, 67–81. [CrossRef]
14. Hashemi, S.; Negarestani, A.; Namvaran, M.; Nasab, S.M.M. An analytical algorithm for designing radon monitoring network to predict the location and magnitude of earthquakes. *J. Radioanal. Nucl. Chem.* **2013**, *295*, 2249–2262. [CrossRef]
15. Petraki, E.; Nikolopoulos, D.; Panagiotaras, D.; Cantzos, D.; Yannakopoulos, P. Radon-222: A Potential Short-Term Earthquake Precursor. *J. Earth Sci. Clim. Chang.* **2015**, *6*, 282. [CrossRef]

16. Rice, J.R. Fault stress states, pore pressure redistributions, and the weakness of the San Andreas fault. In *Fault Mechanics and Transport Properties of Rock*; Evans, B., Wong, T.F., Eds.; Academic Press Ltd.: San Diego, CA, USA, 1992; pp. 476–503.
17. Sibson, R.H. Fluid involvement in normal faulting. *J. Geodyn.* **2000**, *29*, 449–469. [CrossRef]
18. Collettini, C.; Cardellini, C.; Chiodini, G.; De Paola, N.; Holdsworth, R.E.; Smith, S.A.F. Fault weakening due to CO_2 degassing in the Northern Apennines: Short and long-term processes. *Geol. Soc. Lond. Spec. Publ.* **2008**, *299*, 175–194. [CrossRef]
19. King, C.Y.; King, B.S.; Evans, W.C.; Zhang, W. Spatial radon anomalies on active faults in California. *Appl. Geochem.* **1996**, *11*, 497–510. [CrossRef]
20. Annunziatellis, A.; Beaubien, S.E.; Bigi, S.; Ciotoli, G.; Coltella, M.; Lombardi, S. Gas migration along fault systems and through the vadose zone in the Latera caldera (central Italy): Implications for CO_2 geological storage. *Int. J. Greenh. Gas Control* **2008**, *2*, 353–372. [CrossRef]
21. Sciarra, A.; Fascetti, A.; Moretti, A.; Cantucci, B.; Pizzino, L.; Lombardi, S.; Guerra, I. Geochemical and radiometric profiles through an active fault in the Sila Massif (Calabria, Italy). *J. Geoch. Explor.* **2014**, *148*, 128–137. [CrossRef]
22. Mandelbrot, B.B. The fractal geometry of nature. Review by: Cannon, J.W. *Am. Math. Mon.* **1984**, *91*, 594–598. [CrossRef]
23. Perfect, E.; Kay, B.D. Applications of fractals in soil and tillage research: A review. *Soil Till. Res.* **1995**, *36*, 1–20. [CrossRef]
24. Eghball, B.; Hergert, G.W.; Lesoing, G.W.; Ferguson, R.B. Fractal analysis of spatial and temporal variability. *Geoderma* **1999**, *88*, 349–362. [CrossRef]
25. Mandelbrot, B.B. *Fractals: Form, Chance, and Dimension*; W.H. Freeman: San Francisco, CA, USA, 1977; p. 365.
26. Pachepsky, Y.; Crawford, J.W. Fractal analysis. In *Encyclopedia of Soils in the Environment*; Hillel, D., Ed.; Academic Press: Waltham, MA, USA, 2004; Volume 2, pp. 85–98.
27. Allaire, S.E.; Lange, S.F.; Lafond, J.A.; Pelletier, B.; Cambouris, A.N.; Dutilleul, P. Multiscale spatial variability of CO_2 emissions and correlations with physico-chemical soil properties. *Geoderma* **2012**, *170*, 251–260. [CrossRef]
28. Ryu, S.; Concilio, A.; Chen, J.; North, M.; Ma, S. Prescribed burning and mechanical thinning effects on below-ground conditions and soil respiration in a mixed-conifer forest, California. *For. Ecol. Manag.* **2009**, *257*, 1324–1332. [CrossRef]
29. Panosso, A.R.; Perillo, L.I.; Ferraudo, A.S.; Pereira, G.T.; Miranda, J.G.V.; La Scala, N. Fractal dimension and anisotropy of soil CO_2 emission in a mechanically harvested sugarcane production area. *Soil Till. Res.* **2012**, *124*, 8–16. [CrossRef]
30. Burrough, P.A. Fractal dimensions of landscapes and other environmental data. *Nature* **1981**, *294*, 240–242. [CrossRef]
31. Palmer, M.W. Fractal geometry: A tool for describing spatial patterns of plant communities. *Vegetatio* **1988**, *75*, 91–102. [CrossRef]
32. La Scala, N., Jr.; Marques, J., Jr.; Pereira, G.T.; Corà, J.E. Short-term temporal changes in the spatial variability model of CO_2 emissions from a Brazilian bare soil. *Soil Biol. Biochem.* **2000**, *32*, 1459–1462. [CrossRef]
33. Ohashi, M.; Gyokusen, K. Temporal change in spatial variability of soil respiration on a slope of Japanese cedar (Cryptomeria japonica D. Don) forest. *Soil Biol. Biochem.* **2007**, *39*, 1130–1138. [CrossRef]
34. Kosugi, Y.; Mitani, T.; Ltoh, M.; Noguchi, S.; Tani, M.; Matsuo, N.; Takanashi, S.; Ohkubo, S.; Nik, A.R. Spatial and temporal variation in soil respiration in a Southeast Asian tropical rainforest. *Agric. For. Meteorol.* **2007**, *147*, 35–47. [CrossRef]
35. Konda, R.; Ohta, S.; Ishizuka, S.; Aria, S.; Ansori, S.; Tanaka, N.; Hardjono, A. Spatial structures of N_2O, CO_2 and CH_4 fluxes from Acacia mangium plantation soils during a relatively dry season in Indonesia. *Soil Biol. Biochem.* **2008**, *40*, 3021–3030. [CrossRef]
36. Bicalho, E.S.; Panosso, A.R.; Teixeira, D.D.B.; Miranda, J.G.V.; Pereira, G.T.; La Scala, N. Spatial variability structure of soil CO_2 emission and soil attributes in a sugarcane area. *Agric. Ecos. Environ.* **2014**, *189*, 206–215. [CrossRef]
37. Telesca, L.; Lapenna, V.; Macchiato, M. Multifractal fluctuations in seismic interspike series. *Physica A* **2005**, *354*, 629–640. [CrossRef]
38. Chamoli, A.; Yadav, R.B.S. Multifractaly in seismic sequences of NW Himalaya. *Nat. Hazards* **2015**, *77*, s19–s32. [CrossRef]

39. Weinlich, F.H. Carbon dioxide controlled earthquake distribution pattern in the NW Bohemian swarm earthquake region, western Eger Rift, Czech Republic—Gas migration in the crystalline basement. *Geofluids* **2014**, *14*, 143–159. [CrossRef]
40. Fischer, T.; Matyska, C.; Heinicke, J. Earthquake-enhanced permeability–evidence from carbon dioxide release following the ML 3.5 earthquake in West Bohemia. *Earth Planet. Sci. Lett.* **2017**, *460*, 60–67. [CrossRef]
41. Boncio, P.; Lavecchia, G.; Milano, G.; Rozzi, B. Seismogenesis in central Appennines, Italy: An integrated analysis of minor earthquake sequences and structural data in the Amatrice-Campotosto Area. *Ann. Geophys.* **2004**, *47*, 1723–1742.
42. Pace, B.; Peruzza, L.; Lavecchia, G.; Boncio, P. Layered seismogenic source model and probabilistic seismic-hazard analyses in central Italy. *Bull. Seismol. Soc. Am.* **2006**, *96*, 107–132. [CrossRef]
43. Lavecchia, G.; Castaldo, R.; de Nardis, R.; De Novellis, V.; Ferrarini, F.; Pepe, S.; Brozzetti, F.; Solaro, G.; Cirillo, D.; Bonano, M.; et al. Ground deformation and source geometry of the 24 August 2016 Amatrice earthquake (Central Italy) investigated through analytical and numerical modelling of DInSAR measurements and structural-geological data. *Geophys. Res. Lett.* **2016**, *43*. [CrossRef]
44. Brozzetti, F.; Boncio, P.; Cirillo, D.; Ferrarini, F.; de Nardis, R.; Testa, A.; Liberi, F.; Lavecchia, G. High-resolution field mapping and analysis of the August–October 2016 coseismic surface faulting (central Italy earthquakes): Slip distribution, parameterization, and comparison with global earthquakes. *Tectonics* **2019**, *38*. [CrossRef]
45. Blumetti, A.M.; Guerrieri, L. Fault-generated mountain fronts and the identification of fault segments: Implications for seismic hazard assestment. *Boll. Soc. Geol. Ital.* **2007**, *126*, 307–322.
46. Festa, A. Geometrie e meccanismi di raccorciamento nel settore meridionale del Bacino marchigiano (Monte Gorzano, Appennino centrale). *Ital. J. Geosci.* **2005**, *124*, 41–51.
47. Chiodini, G.; Cioni, R.; Guidi, M.; Raco, B.; Marini, L. Soil CO_2 flux measurements in volcanic and geothermal areas. *Appl. Geochem.* **1998**, *13*, 543–552. [CrossRef]
48. Vidal Vazquez, E.; Miranda, J.G.V.; Paz González, A. Characterizing anisotropy and heterogeneity of soil surface microtopography using fractal models. *Ecol. Model.* **2005**, *182*, 337–353. [CrossRef]
49. Huang, C.H.; Bradford, J.M. Applications of a laser scanner to quantify soil microtopography. *Soil Sci. Soc. Am. J. Abstr.* **1992**, *56*, 14–21. [CrossRef]
50. Lewicki, J.L.; Evans, W.C.; Hilley, G.E.; Sorey, M.L.; Rogie, J.D.; Brantley, S.L. Shallow soil CO_2 flow along the San Andreas and Calaveras Faults, California. *J. Geophys. Res.* **2003**, *108*. [CrossRef]
51. Walia, V.; Lin, S.J.; Fu, C.C.; Yang, T.F.; Hong, W.L.; Wen, K.L.; Chen, C.H. Soil-gas monitoring: A tool for fault delineation studies along Hsnhua Fault (Tainan), Southern Taiwan. *App. Geoch.* **2010**, *25*, 602–607. [CrossRef]
52. Jung, B.; Garven, G.; Boles, J.R. Effects of episodic fluid flow on hydrocarbon migration in the Newport-Inglewood Fault Zone, Southern California. *Geofluids* **2014**, *14*, 234–250. [CrossRef]
53. Concilio, A.; Chen, J.Q.; Ma, S.; North, M. Precipitation drives interannual vari- ation in summer soil respiration in a Mediterranean-climate, mixed-conifer forest. *Clim. Chang.* **2009**, *92*, 109–122. [CrossRef]
54. Cantero, J.J.; Leon, R.; Cisneros, J.M.; Cantero, A. Habitat structure and vegetation relationships in central Argentina salt marsh landscapes. *Plant Ecol.* **1998**, *137*, 79–100. [CrossRef]
55. Tavares, R.L.M.; Souza, Z.M.; La Scala, N., Jr.; Castioni, G.A.F.; Souza, G.S.; Torres, J.L.T. Spatial and Temporal Variability of Soil CO_2 Flux in Sugarcane Green Harvest Systems. *Rev. Bras. Cienc. Solo* **2016**, *40*. [CrossRef]
56. Nikolopoulos, D.; Petraki, E.; Yannakopoulos, P.; Cantzos, D.; Panagiotaras, D.; Nomicos, C. Fractal Analysis of Pre-Seismic Electromagnetic and Radon Precursors: A Systematic Approach. *J. Earth Sci. Clim. Chang.* **2016**, *7*. [CrossRef]
57. Nikolopoulos, D.; Petraki, E.; Vogiannis, E.; Chaldeos, Y.; Yannakopoulos, P.; Kottou, S.; Nomicos, C.; Stonham, J. Traces of self-organisation and long-range memory in variations of environmental radon in soil: Comparative results from monitoring in Lesvos Island and Ileia (Greece). *J. Radioanal. Nucl. Chem.* **2014**, *299*, 203–219. [CrossRef]
58. Petraki, E.; Nikolopoulos, D.; Chaldeos, Y.; Koulouras, G.; Nomicos, C.; Yannakopoulos, P.; Kottou, S.; Stonham, J. Fractal evolution of MHz electromagnetic signals prior to earthquakes: Results collected in Greece during 2009. *Geomat. Nat. Hazards Risk* **2016**, *7*, 550–564. [CrossRef]
59. Nikolopoulos, D.; Matsoukas, C.; Yannakopoulos, P.; Petraki, E.; Cantzos, D.; Nomicos, C. Long-Memory and Fractal Trends in Variation of Environmental Radon in Soil: Results from Measurements in Less Island in Greece. *J. Earth Sci. Clim. Chang.* **2018**, *9*, 1–11.

60. Nikolopoulos, D.; Petraki, E.; Nomicos, C.; Koulouras, G.; Kottou, S.; Yannakopoulos, P. Long-memory trends in disturbances of radon in soil prior to the twin ML = 5.1 earthquakes of 17 November 2014 Greece. *J. Earth Sci. Clim. Chang.* **2015**, *6*, 1–10.
61. Italiano, F.; Bonfanti, P.; Ditta, M.; Petrini, R.; Slejko, F. Helium and carbon isotopes in the dissolved gases of Friuli Region (NE Italy): Geochemical evidence of CO_2 production and degassing over a seismically active area. *Chem. Geol.* **2009**, *266*, 76–85. [CrossRef]
62. Quattrocchi, F.; Pizzi, A.; Gori, S.; Boncio, P.; Voltattorni, N.; Sciarra, A. The contribution of fluid geochemistry to define the structural patterns of the 2009 L'Aquila seismic source. *Ital. J. Geosci.* **2012**, *131*, 448–458. [CrossRef]
63. Martinelli, G.; Plescia, P. Mechanochemical dissociation of calcium carbonate: Laboratory data and relation to natural emission of CO_2. *Phys. Earth Planet. Inter.* **2004**, *142*, 205–214. [CrossRef]